

Full paper

# Biomimetic printable nanocomposite for healable, ultrasensitive, stretchable and ultradurable strain sensor

Yang Liu<sup>a</sup>, Xinlei Shi<sup>a</sup>, Shuiren Liu<sup>a</sup>, Hongpeng Li<sup>a</sup>, Huailong Zhang<sup>a</sup>, Conghui Wang<sup>a</sup>, Jiajie Liang<sup>a,b,c,\*</sup>, Yongsheng Chen<sup>b</sup>

<sup>a</sup> School of Materials Science and Engineering, National Institute for Advanced Materials Nankai University, Tianjin, 300350, PR China

<sup>b</sup> Key Laboratory of Functional Polymer Materials of Ministry of Education, College of Chemistry, Nankai University, Tianjin, 300350, PR China

<sup>c</sup> Tianjin Key Laboratory of Metal and Molecule-Based Material Chemistry and Collaborative Innovation Center of Chemical Science and Engineering (Tianjin), Nankai University, Tianjin, 300350, PR China

## ARTICLE INFO

## Keywords:

Healable sensor  
Ultrasensitive  
Durable  
Hierarchical structure  
Printable nanocomposite

## ABSTRACT

The trend towards progressively more portable and wearable strain sensors has led to rapid advancement in full-range human-health diagnostics. However, developing sensing materials with long-term durability and lifetime, while maintaining high sensitivity and large working range, remains a grand challenge. Herein, we design a printable nanocomposite with nacre-inspired hierarchical structure, diffusible components and abundant dynamic interactions for the construction of healable and durable strain sensor. In contrast to conventional hydrogel and elastomer-based healable sensing materials, this nanocomposite can simultaneously exhibit gauge factor > 100 over full range of working strains up to 52% and demonstrate an ultrahigh gauge factor exceeding 3500 in the strain region of 38–52%. This strain sensor can repeatedly and effectively self-heal with simple water treatment, greatly expanding its lifespan and cycling durability (over 10,000 cycles). The healed device can completely restore its sensing ability for precise full-range human-body monitoring. Our strategy represents a critical step in the continual development of wearable electronics.

## 1. Introduction

In the recent decade, wearable electronics have cemented their legacy as one of the key components in the growing field of Internet of Things (IoT) technology [1–4]. In medical diagnostic systems, skin-mountable strain sensors, which transduce mechanical stimuli into an electrical output, represent an avenue for real-time, non-invasive tracking [5]. For these strain sensors to be viable for full-range human-health diagnostics and human-body tracking, the sensor must possess high sensitivity (defined by its gauge factor), large stretchability (defined as the maximum working strain), and long-term operational durability (or cycling lifetime) [6,7]. In recent years, though much work has focused on improving the sensitivity or broadening the working strain range of the sensor [8–11], few studies have been conducted on improving the operational lifetime and durability of the strain sensor [7]. However, our day-to-day activity results in multitudes of opportunities for skin-mountable electronics to become susceptible to unexpected ruptures or undesired scratches. These unintended consequences would drastically reduce the device lifetime, mandating costly and impractical maintenance of the device [12]. To enable these

wearable strain sensors for practical applications, it is imperative to develop methods to enhance their robustness and durability, while maintaining their sensing properties.

Self-healing is a concept drawn from nature, in which materials can revert to their original state with a full or partial recovery of functionality after damage. This concept has garnered increasing interest in the development of highly durable and sustainable wearable electronics [13,14]. Human skin can be viewed as the paradigm, as this remarkable and integral bodily component can repeatedly repair itself while maintaining highly durable mechanical and sensory properties [15]. Motivated in part by this particular appendage, the strategy of incorporating healable capability into electronic applications represents one avenue to expand the operational lifetime and durability of strain sensors. To date, electrically and ionically conductive components have been used in conjunction with polymeric hydrogel or elastomer with self-healing abilities to create healable strain and pressure sensors [16–18]. While these ultra-soft sensors exhibit reliable and repeatable self-recovery ability, with stretchability usually exceeding 100% [15,19], they suffer from two fundamental issues that hinder their adaptation into practical applications. First, hydrogel-based materials contain large

\* Corresponding author. School of Materials Science and Engineering, National Institute for Advanced Materials Nankai University, Tianjin, 300350, PR China.  
E-mail address: [liang0909@nankai.edu.cn](mailto:liang0909@nankai.edu.cn) (J. Liang).

amounts of water that leach and evaporate easily, resulting in time dependent performance of hydrogel properties [20,21]. Secondly, these sensors typically exhibit low sensitivities, making it difficult to accurately detect and distinguish weak and complicated signal waves arising from the human body [7,16].

The healing process for polymeric healable materials typically comprises three critical steps: 1) the broken segments of the interface are able to come into intimate contact with each other; 2) the polymer chains migrate and diffuse along the damaged interface; and 3) dynamic interactions (i.e. hydrogen bonding, ionic bonding, covalent bonding, and guest-host interaction) can reconstruct at the damaged interface [22,23]. To enable these three steps, the polymer chains in the healable materials must possess sufficient mechanical flexibility and compliance to enable the interdiffusion and re-entanglements of polymer chains at the damaged areas [24]. Unfortunately, while this high polymer chain mobility is conducive to achieving large working strain ranges, there exists a tradeoff with the structural requirements for high sensitivity [25-27]. To realize high sensitivity, mechanical brittleness is desired to enable the sensing materials to realize substantial structural changes under nuanced strain [25]. This thus presents a dichotomy between the healing ability and mechanical brittleness for the hydrogel or rubber-based sensing materials.

To resolve the dichotomy between sensitivity and stretchability, we previously proposed a novel design for ultrasensitive and stretchable strain sensors utilizing a nacre-mimetic microscale “brick-and-mortar” architecture. In this design, the synergistic effects between the inorganic “brick” and organic “mortar” not only allow for controlled crack generation to ensure high sensitivity, but also dissipate considerable loading energy via rich interfacial interactions, layer slippage, and molecular chain stretching to guarantee large stretchability [28-35]. As a result, the highest reported gauge factor to date ( $> 8700$ ) and the ability to work in a strain range broader than 80% was demonstrated [36]. To build on the success of this previous design, this work aims to integrate healing abilities while retaining all aforementioned attributes of the “brick” and “mortar” design. As per before, the critical consideration lies with the material selection for the “brick” and “mortar” material. For the “brick” material, graphene oxide (GO) nanosheets have been reported to exhibit water-initiated, self-healing properties by virtue of their rich oxygen-containing functional groups which form abundant dynamic hydrogen bonds [33-35,37]. This functionality allows the nanosheet assemblies to restore their microstructure and mechanical properties after being subjected to moisture [37]. For the “mortar” material, poly(vinyl alcohol) (PVA) hydrogel has developed a reputation as one of the self-healing hydrogels most suitable for bioremediation applications [38]. This self-healing ability of PVA-based hydrogels is attributed largely in part to the mobility of the PVA chain which facilitates the diffusion of PVA. Furthermore, the high concentration of free hydroxyl groups on PVA chains enables the rebuilding of hydrogen bonds after being damaged [38,39]. As such, these materials in synergistic harmony foreshadow the development of healable sensors capable of achieving the comprehensive performance mandated of strain sensors.

Based on these considerations, in this work, the design and construction of a printed nanocomposite-based strain sensor with “brick-and-mortar” hierarchical architecture, diffusible components, and abundant dynamic interactions is presented which integrates the seemingly contradictory functionalities of effectively healing, large stretchability, and high sensitivity. The resultant skin-mountable and healable strain sensor comprises GO nanosheets and silver nanowires (AgNWs) as the “brick” material, and traces of PVA/Ca<sup>2+</sup> as the “mortar” material. The AgNW network provides the high conductivity required of the sensing system, while the GO nanosheets endow the system with mechanical brittleness and rich functional groups, and the PVA ignites the mechanical toughening and healing effects through abundant interfacial hydrogen bonding and polymer chain movement. In addition, the introduction of Ca<sup>2+</sup> ions results in the formation of

strong and dynamic coordination bonding with PVA and GO, which can significantly enhance the re-healing ability of the sensing system. With the cohesive performance of all individual materials, the resulting strain sensor is able to demonstrate a working strain range broader than 50%, with ultrahigh sensitivity throughout the entirety of the working strain range (gauge factor of 105.3, 567.0, 1210.7, and 3564.5 in the strain regions of 0-10, 10-28, 28-38, and 38-52%, respectively). Furthermore, the sensor exhibits water-initiated healing properties, with the repaired devices outputting similar sensing and cycling performances as those of the original device even after multiple breaking and healing cycles. This ability of repeatable repair can greatly expand the operational durability and cycling lifetime of the strain sensor. To the best of the authors’ knowledge, this represents the first realization of healable strain sensors that integrates effective healing capability (high healing efficiency over multiple breaking/healing cycles), large stretchability (working strain range  $> 50\%$ ), high sensitivity (gauge factor  $> 100$  over the entire working strain range), and good durability. These performance metrics represent a solid step toward the practical application of wearable strain sensors.

## 2. Experimental section

### 2.1. Raw materials

AgNWs were synthesized with an average diameter of 40 nm and a length of 20  $\mu\text{m}$ . Poly(vinyl alcohol) (PVA) was purchased from Alfa Aesar (98–99% hydrolyzed, Mw  $\sim 130,000$ ). Calcium chloride was obtained from Beijing Dingguo bio-tech Co., Ltd (Beijing, China). Polyurethane (4055IC) was sourced from Yantai Wanhua Polyurethane Co., Ltd. Deionized water was used throughout the work. The giant GO was prepared via the modified Hummers’ method.

### 2.2. Preparation of GO-AgNW/PVA-Ca<sup>2+</sup> gel-like ink

In a typical preparation, 2 mg/mL GO dispersion was made by first dispersing GO in distilled water via sonication for 30 min. After sonication, the pH value was adjusted to 6.5 by adding 0.2 M NaOH aqueous solution. Subsequently, the AgNW solution was added into the GO solution at a AgNW to GO weight ratio of 20:2.5. After sonication for 10 min, the AgNW and GO mixture was vacuum filtrated using a PTFE membrane filter with a pore size of 0.45  $\mu\text{m}$  and washed with 200 mL of distilled water. The resulting precipitate was redispersed in distilled water through strong agitation using a VORTEX mixer at 1000 rpm for 2 h to obtain the final homogeneous GO-AgNW (mass ratio of GO:AgNW = 5:40) ink. 10 mg/mL PVA aqueous solution was added to the ink at a weight ratio 5:100, followed by addition of 1 mg/mL CaCl<sub>2</sub> aqueous solution to a final mass ratio AgNW:GO:PVA:Ca<sup>2+</sup> = 40:5:0.25:0.05. GO-AgNW/PVA (GO:AgNW:PVA = 5:40:0.25) and GO-AgNW/Ca<sup>2+</sup> (GO:AgNW:Ca<sup>2+</sup> = 5:40:0.05) ink were also prepared without addition of CaCl<sub>2</sub> and PVA, respectively.

### 2.3. Construction of the strain sensor

The strain sensor was fabricated through a screen-printing technique, with the printing force, speed, and angle between the squeegee and stencil optimized specifically for the GO-AgNW based inks. The screen-printing plate with the appropriate pattern was first installed in the screen-printing machine (TC-4060k screen printer, Dongguan Ta Chen Screen Printing Machine & Materials Co., Ltd.). Following installation, the gel was spread onto the screen-printing plate and printed by sliding the squeegee over the stencil. After printing, the sensor patterns were dried under ambient conditions for 3-5 min to evaporate the water before tests were conducted. The thickness of the strain sensor could be adjusted by changing the weight percentage of the DI water. All electromechanical measurements were conducted parallel to width direction.

## 2.4. Characterization

The resistance change was measured with a Keithley 2000 digital multimeter. Stretching tests and cyclic strain tests were performed on a motorized linear stage with built-in controller (Zolix Inc.). Strain and resistance data were recorded with a custom-made LabView code. The morphology and mapping of the GO-AgNW/PVA-Ca<sup>2+</sup> nanocomposite film was imaged using a JSM-7800 SEM machine. Silver nanowires were analyzed through TEM images taken from a JEM-2800 system. XPS characterization was conducted using an ESCALAB 250Xi system from Thermo Scientific. X-ray diffraction (XRD) measurements were carried out using a Rigaku D/Max-2500 diffractometer with Cu-K $\alpha$  radiation. The functional groups of the specimens were recorded on a BRUKER TENSOR27 FT-IR spectrometer in the 4000–400 cm<sup>-1</sup> range. A total of 60 scans were averaged to yield the final spectra with a resolution of 2 cm<sup>-1</sup>. Rheological behavior of the formulated inks was probed using a DHR-2 rheometer (TA Instruments) with a 25 mm plate system and 900  $\mu$ m gap. All of the tested ink samples were tested under the same solid content and at room temperature (25 °C). A preconditioning step at a shear rate of 0.1 s<sup>-1</sup> for 10 s was applied prior to each test. A steady-state flow step test was performed to measure the shear viscosity of the inks at shear rates of 0.1–1000 s<sup>-1</sup>, and a peak hold step test was performed with constant shear rates in three intervals (0.1 s<sup>-1</sup> shear rate for 60 s, 200 s<sup>-1</sup> for 60 s, and 0.1 s<sup>-1</sup> for 130 s) to simulate the screen-printing process. The stress sweep step test was performed with an oscillation stress of 1–1000 Pa at a frequency of 1 Hz.

## 3. Results and discussion

To generate a baseline comparison, a GO-AgNW nanocomposite-based strain sensor without the addition of any organic “mortar” material was first prepared. The addition of AgNWs to the GO electrode greatly increases the conductivity of the resultant sensing material without any deleterious effects to its mechanical properties [40,41]. This property is critical in improving the gauge factor of the strain sensor and essential for sensing applications requiring low power consumption [42]. To elucidate the impact of the “mortar” material, GO-AgNW/PVA, GO-AgNW/PVA-Ca<sup>2+</sup> and GO-AgNW/Ca<sup>2+</sup> strain sensors were further fabricated. The addition of Ca<sup>2+</sup> is for the ability of the material to form strong, yet dynamic coordination interactions with both GO and PVA, which results in enhanced mechanical strength and toughness of the nanocomposite materials [33,43]. Briefly, all strain sensors were fabricated by formulating the corresponding viscous and shear-thinning nanocomposite gel (Fig. S1). Following the gel formulation, the resultant material was directly screen printed onto stretchable polyurethane substrates according to our previously reported method (Fig. 1a) [41]. To ensure good adhesion between the sensing material and the stretchable substrate, an O<sub>2</sub> plasma treatment was used on the polyurethane surface to improve hydrophilicity prior to the nanocomposite gel printing.

Cross-sectional scanning electron microscopy (SEM) images of the fracture edges of the strain sensors with and without “mortar” materials are depicted in Fig. 1c and Fig. S2 and clearly illustrate the microscale layered structure in addition to the uniformly distributed AgNWs (Fig. 1d). As a result of the high conductivity of the AgNWs, all lamellar strain sensors exhibit electrical conductivities exceeding 6000 S/cm (Fig. S3). For the GO-AgNW/PVA-Ca<sup>2+</sup> strain sensors, energy-dispersive X-ray spectroscopy (EDS) was used to confirm the existence and uniformity of the distribution of Ca<sup>2+</sup> (Fig. 1e). The X-ray diffraction (XRD) patterns of the pure GO, GO-PVA and GO-Ca<sup>2+</sup> nanocomposite films exhibit typical diffraction peaks for *d*-spacing of GO at  $\sim$ 12.7°, 12.1° and 11.7° respectively (Fig. 1f). Obviously, after adding PVA or Ca<sup>2+</sup>, the spacing between GO nanosheets in both GO-PVA and GO-Ca<sup>2+</sup> nanocomposite films increases, which is strong evidence of the successful intercalation of PVA or Ca<sup>2+</sup> into the GO nanosheets [33,43].

Because of the multitude of oxygen-containing groups on the surface

and edge of the GO nanosheets, GO nanosheets can form strong interfacial interactions with PVA chains through hydrogen bonding [43–45]. The Fourier-transformed infrared spectrum (FT-IR) of pure GO films and GO-Ca<sup>2+</sup> films show the C=O stretch and epoxy/ether C-O stretch at  $\sim$ 1730 cm<sup>-1</sup> and 1260 cm<sup>-1</sup>, respectively (Fig. 1g) [46]. However, the intensities of both of these bonds are significantly decreased in the case of the GO-Ca<sup>2+</sup> film, in line with previously reported results [33,47]. The decrease in C=O stretch intensity can be attributed to carboxylic acid coordinated to Ca<sup>2+</sup> [33,48,49]. Furthermore, the Lewis acidic Ca<sup>2+</sup> can lead to ring-opening of epoxides to create C-OH moieties, which leads to further coordination [33,48,49]. Another observation from the FT-IR spectrum is the red-shifting of the –OH bending vibration in the PVA-Ca<sup>2+</sup> from 1452 and 1378 cm<sup>-1</sup> to 1427 and 1284 cm<sup>-1</sup>, respectively, when compared to the pure PVA spectra. This red-shifting is further evidence of the coordination effect of Ca<sup>2+</sup> with C-OH moieties in PVA [50–52]. X-ray photoelectron spectroscopy (XPS) provides further validation of the formation of coordination bonds in the GO-Ca<sup>2+</sup> and PVA-Ca<sup>2+</sup> films. Compared to the Ca 2p spectra in pure CaCl<sub>2</sub> (348.1 eV, Ca 2p<sub>1/2</sub> and 351.6 eV, Ca 2p<sub>3/2</sub>), both Ca 2p<sub>1/2</sub> and Ca 2p<sub>3/2</sub> peaks observed in the GO-Ca<sup>2+</sup> and PVA-Ca<sup>2+</sup> composites show a slight shift (Fig. 1h) due to the coordination between the Ca<sup>2+</sup> and the oxygen-containing groups in GO and PVA [53]. These results suggest that hydrogen and coordination bonds are the dominating interfacial interactions in GO-AgNW/PVA-Ca<sup>2+</sup> strain sensors.

The impact of the “mortar” material on the sensing performance was evaluated by fabricating strain sensors with a length of 20 mm, a width of 3 mm, and a thickness of  $\sim$ 800 nm. The resulting strain sensors were mounted on a linear motorized stage connected to a Keithley 2000 digital multimeter to record resistance changes during the stretching and releasing processes. In this setup, the uniaxial strain range is controlled by the linear stage, and the sensitivity (gauge factor) of the strain sensors is determined by the change in relative electrical resistances  $((R - R_0)/R_0)$ . All samples were subjected to a 20% pre-strain before conducting the sensing performance test. The typical resistance change as a function of applied strain for one stretch and release cycle is presented in Fig. 2a. While the GO-AgNW standalone sensor possesses a high sensitivity (gauge factor of 3379, as seen in Fig. S4a), it has a limited working strain range of 38%. On the other hand, the GO-AgNW/PVA strain sensor bridged with the PVA “mortar” has a broader working strain range up to 70%, but comes at the expense of the sensitivity value (gauge factor of 1324, as seen in Fig. S4b). These results are indicative of the improvement in the stretchability of the strain sensor, which allows the sensor to accommodate higher applied stress though the synergistic toughening effects of polymer chain movement and breakage of interfacial hydrogen bonding [54–56]. However, the enhanced stretchability also compromises the sensing material's mechanical brittleness [10,42,57].

While the addition of PVA was observed to only improve stretchability, the addition of Ca<sup>2+</sup> was observed to enhance both the stretchability (working strain up to 44%) and sensitivity (gauge factor up to 7790.2) of the sensing materials, as seen in Fig. S4c. This simultaneous enhancement of both parameters is due to the introduction of strong interactions between the Ca<sup>2+</sup> and oxygen functional groups on the basal planes and carboxylate groups on the edges of the GO nanosheets [33]. When all materials were integrated together in the GO-AgNW/PVA-Ca<sup>2+</sup> strain sensor, significant enhancement in both stretchability and sensitivity is observed, as seen in Fig. 2b. The sensing curve of this strain sensor features four linear regions: 0–10% with a linearity of 0.979; 10–28% with a linearity of 0.994; 28–38% with a linearity of 0.992; and 38–52% with a linearity of 0.997. The gauge factor corresponding to these regions are 105.3, 567.0, 1210.7, and 3564.5, respectively, representing a strain sensor with a gauge factor exceeding 100 over a working strain range larger than 50%. These performance metrics can be attributed to the hierarchical “brick-and-mortar” structure of the sensor, PVA chain movement, and abundant interfacial interactions within the architecture [30,36,58,59]. The

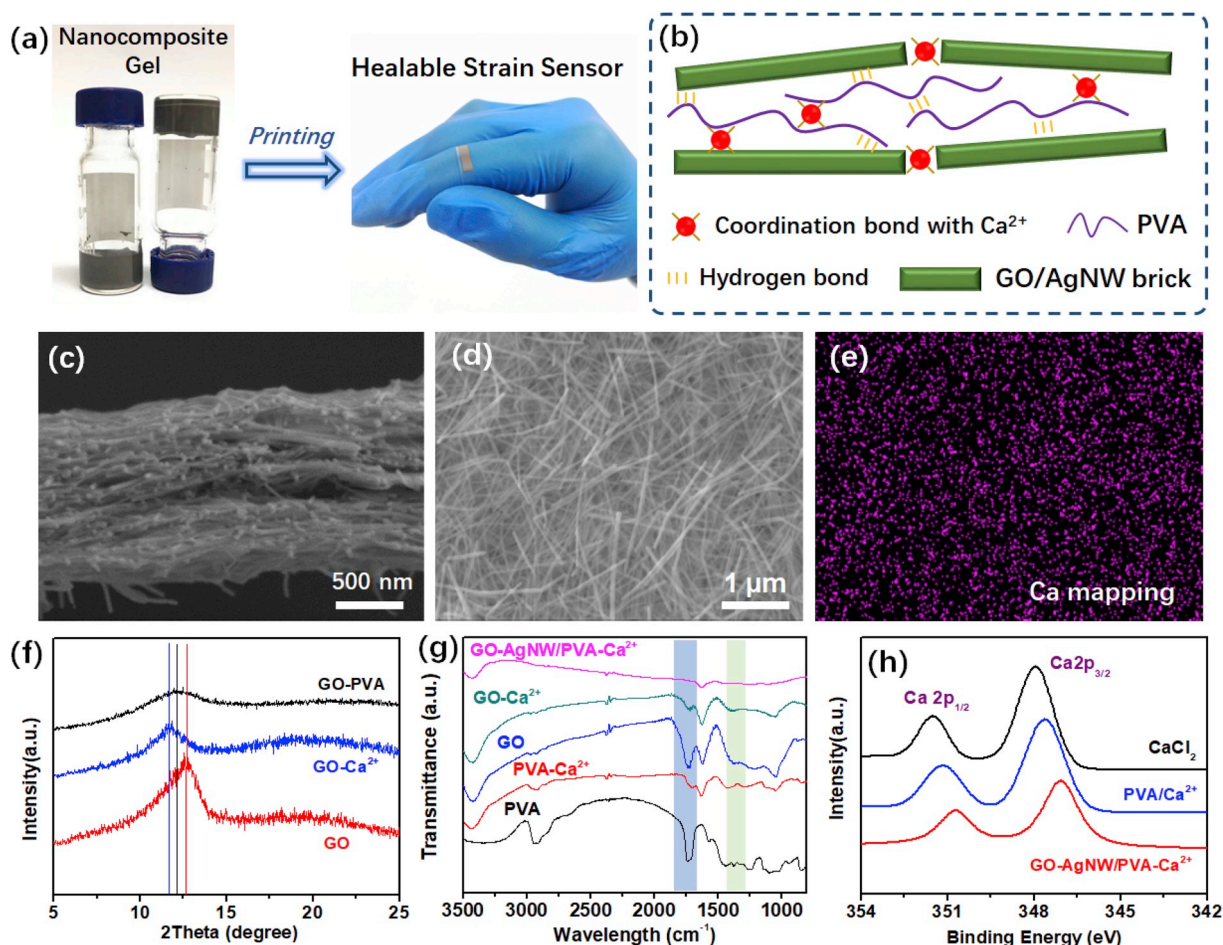


**Fig. 1.** Overview of the fabrication, structure and morphology of the healable strain sensor (a) Schematic of the fabrication process of the GO-AgNW/PVA- $\text{Ca}^{2+}$  strain sensor. (b) Schematic model of the interfacial interactions between GO, PVA and  $\text{Ca}^{2+}$  in the GO-AgNW/PVA- $\text{Ca}^{2+}$  strain sensor. (c) Cross-sectional and (d) top-view SEM images of the GO-AgNW/PVA- $\text{Ca}^{2+}$  sensing film. (e) Corresponding EDS mapping of Ca in the GO-AgNW/PVA- $\text{Ca}^{2+}$  sensing material. (f) XRD patterns for pure GO, GO-PVA, and GO- $\text{Ca}^{2+}$  sensing materials. (g) FT-IR spectra of PVA, PVA- $\text{Ca}^{2+}$ , GO, GO- $\text{Ca}^{2+}$ , and GO-AgNW/PVA- $\text{Ca}^{2+}$  sensing materials. (h) XPS spectrum illustrating the two main peaks Ca  $2p_{1/2}$  and Ca  $2p_{3/2}$  for the pure  $\text{CaCl}_2$ , PVA- $\text{Ca}^{2+}$ , and GO-AgNW/PVA- $\text{Ca}^{2+}$  sensing materials.

brittle nature of the layered structures formed by the “brick” GO and AgNW leads to crack formation and subsequent propagation throughout the entire sensing film during the stretching process (Fig. S5), thus ensuring large conduction changes over the working strain range. The  $\text{Ca}^{2+}$  forms strong coordination bonding between the functional group of the GO nanosheets and the PVA chains, which enhances both the mechanical strength and toughness of the nanocomposite film [60,61]. The hydrogen and coordination-bond breakage, polymer chain movement, and “brick” layer slippage, allows the film to accommodate applied stress during the stretching process, mitigating crack propagation and subsequently enhancing the stretchability [25,28–32,34–36,62,63].

In addition to stretchability and sensitivity, the reliability of the sensing mechanism was also investigated. Fig. 2c illustrates the relative resistance change of the GO-AgNW/PVA- $\text{Ca}^{2+}$  strain sensor at different strain rates between 0–40% applied strain. The electrical responses under the maximum strain of 40% show no dependency on strain rate and remain steady as the stretching rate increases from 1 to 8 mm/s. The relative resistance change under different cyclic strains at a constant strain rate of 2 mm/s is illustrated in Fig. 2d. At strains of 5%, 15%, 30%, and 45%, the corresponding peak percentage in the relative resistances were measured to be about 400, 4400, 16000, and 38000, respectively, which is consistent with the values obtained for one cycle of stretching and releasing. Moreover, the strain sensor can work effectively and reliably under both dry and wetting conditions thanks to the utilization of graphene oxide and PVA as the “brick” and “mortar”

materials respectively. This added validation of the reliability of the strain sensor is critical for commercial applications of this technology for human-health diagnostics and human-motion tracking.

To gauge the practical applicability of the strain sensors, the cyclic durability and healing ability of the strain sensors were evaluated with and without “mortar” materials. To characterize the healing efficiency of the strain sensor, a preconditioning step of stretching and releasing between 0 and 15% at a constant strain rate of 2 mm/s was first conducted to stabilize the sensing performance. Following this preconditioning step, 2x the maximum working strain range was applied to each corresponding strain sensor (i.e., 76% strains applied on the GO-AgNW strain sensors) to damage the sensing material and induce abnormal performance. After operating in this malfunctioned state between 0 and 15% strain for certain cycles, a small amount of de-ionized water (DI water) was dropped onto the broken devices, followed by annealing and drying at 80 °C for 10 min to initiate the healing process. These water-treated devices were again subjected to the same stretching and releasing cycles to assess their healing efficiency, with specific overstretch-to-break/water-treatment-to-heal (henceforth denoted as breaking/healing) cycles performed on different strain sensors corresponding to their specific constituents. The overall testing process for the GO-AgNW standalone strain sensor is depicted in Fig. 3a. For this sensor, the peak variation in the relative resistance was found to be stable at 1,400 during the first 300 cycles of stretching and releasing. To break the sensing film, the film was stretched to 76% strain, resulting in

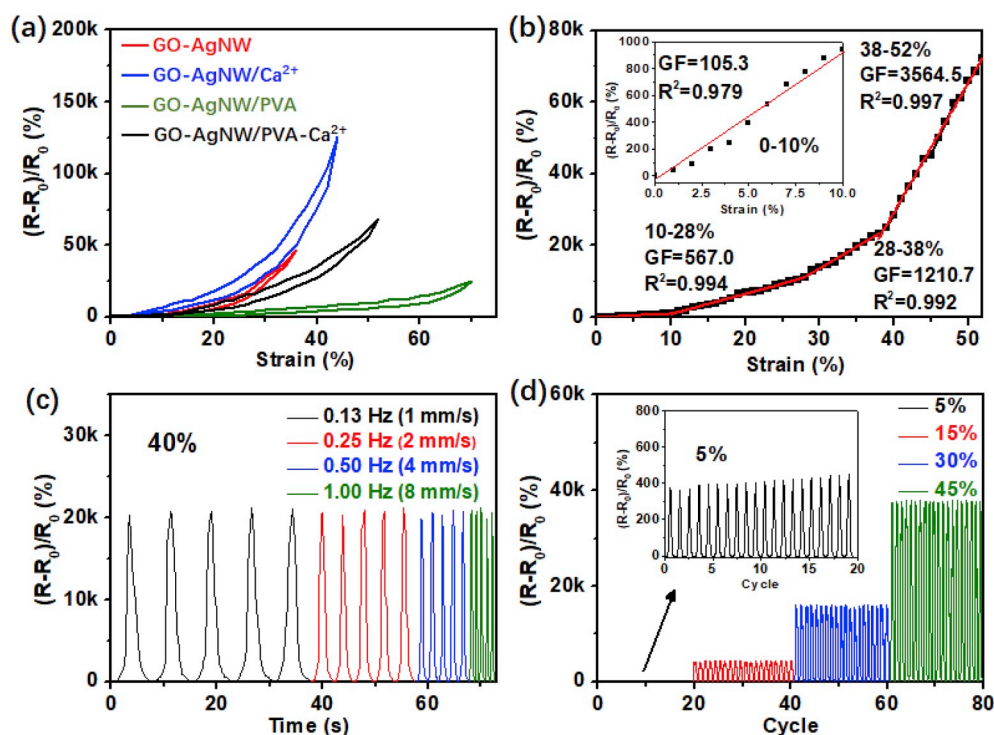


Fig. 2. Sensing behavior of the healable strain sensor. (a) Normalized resistance change as a function of applied strain during one stretch and release cycle for the GO-AgNW, GO-AgNW/PVA, GO-AgNW/PVA-Ca<sup>2+</sup>, and GO-AgNW/Ca<sup>2+</sup> strain sensors. (b) Detailed gauge factor and linear behavior of the GO-AgNW/PVA-Ca<sup>2+</sup> strain sensor. (c) Relative resistance changes of the GO-AgNW/PVA-Ca<sup>2+</sup> strain sensor at different strain rates between 0-40% strain. (d) Relative resistance variations under various cyclical maximum strains (5, 15, 30, and 45%) for the GO-AgNW/PVA-Ca<sup>2+</sup> strain sensor at a strain rate of 2 mm/s.

rapidly fluctuating increases of peak values with increasing cycle numbers. After a water-treatment process, the broken GO-AgNW strain sensor remained malfunctioned state during further cycles of stretching and releasing. Following testing of the GO-AgNW sensor, the GO-AgNW/Ca<sup>2+</sup> strain sensor was tested in the same fashion, and also observed to be incapable of healing malfunctioning devices (Fig. 3b). However, when the sensing materials were bridged with PVA, the water-treatment process enabled the broken GO-AgNW/PVA strain sensor to recover its original electrical response during subsequent stretching and releasing cycles under 0-15% strain (Fig. 3c). These results suggest that the PVA “mortar” is critical for healing the strain

sensor. However, though the strain sensor demonstrated healing abilities, the healed sensor was spontaneously damaged after an additional 320 cycles between 0-15%. Although an additional water-treatment was deemed effective in healing the broken device again, the re-healed GO-AgNW/PVA sensor had a significantly reduced lifetime and completely failed for the third time after only two breaking and healing cycles (Fig. 3c).

The last testing process was conducted with both PVA and Ca<sup>2+</sup> incorporated in the strain sensor. Fig. 4a illustrates the cycling and healing performance of the GO-AgNW/PVA-Ca<sup>2+</sup> strain sensor after five cycles of breaking and healing. In each cycle, the healing process

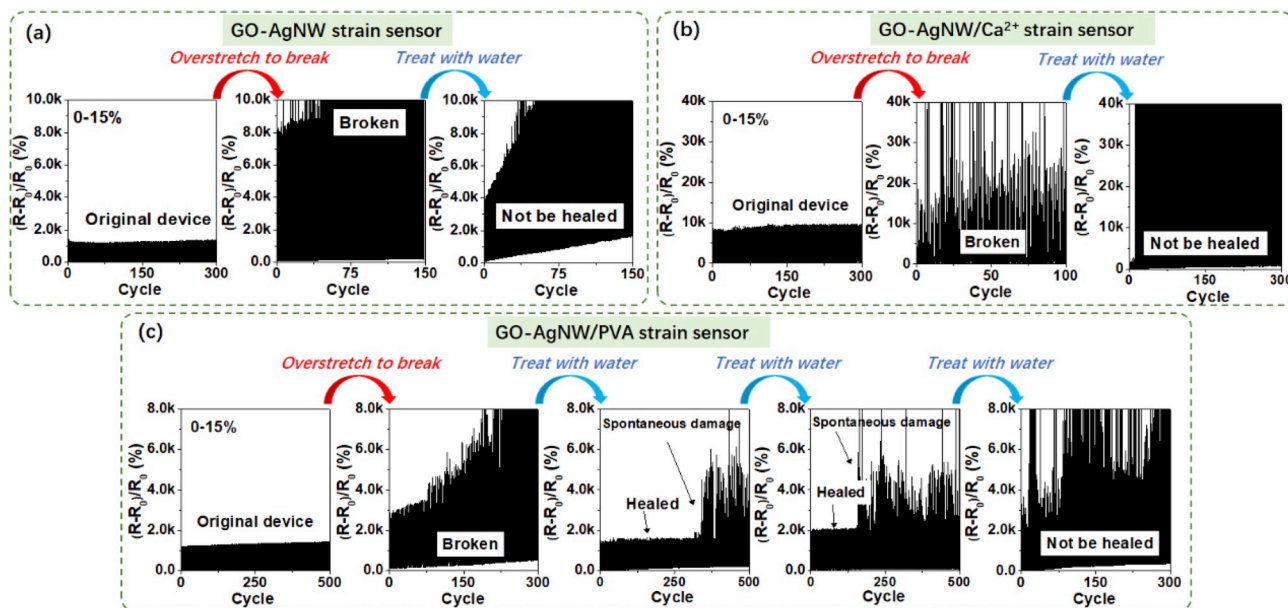
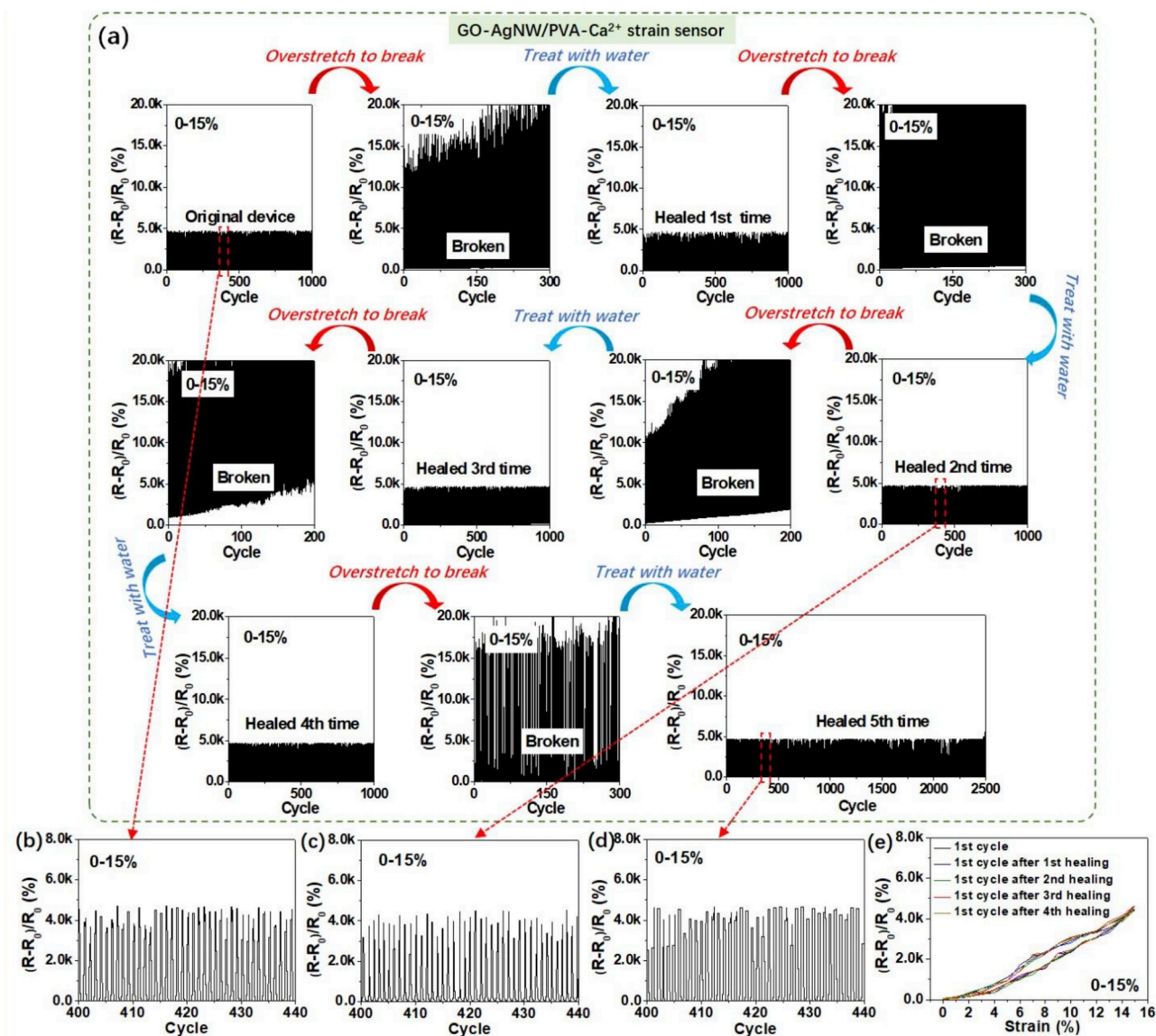


Fig. 3. Healing ability test for GO-AgNW, GO-AgNW/Ca<sup>2+</sup> and GO-AgNW/PVA strain sensors. (a) GO-AgNW, (b) GO-AgNW/Ca<sup>2+</sup> and (c) GO-AgNW/PVA strain sensors strains ranging from 0-15%.



**Fig. 4.** Healing ability test for GO-AgNW/PVA-Ca<sup>2+</sup> strain sensor (a) Cyclic durability and healing ability of the GO-AgNW/PVA-Ca<sup>2+</sup> strain sensor under 0–15% strain. The device was subjected to 5 breaking and healing cycles. Detailed relative resistance change curves recorded between 400 and 440 stretching/releasing cycles for the GO-AgNW/PVA-Ca<sup>2+</sup> strain sensor (b) before being broken, (c) after being subjected to two breaking and healing cycles, and (d) after being subjected to five breaking and healing cycles. (e) Detailed relative resistance changes as a function of strain curves for the specific stretching and releasing cycles corresponding to panel a: 1st cycle before being broken, 1st cycle after being subjected to one breaking and healing cycle, 1st cycle after being subjected to two breaking and healing cycles, 1st cycle after being subjected to three breaking and healing cycles, and 1st cycle after being subjected to four breaking and healing cycles.

remained the same as the aforementioned process with DI water treatment followed by annealing at 80 °C for 10 min. The initial peak value of the relative resistance measured over 1000 cycles of stretching under 15% strain was 4000. After each breaking process, the peak values showed significant variation upon continual cyclical stretching. Following the breaking and healing process, the peak resistance was observed to revert back to the original value of ~4000 over the subsequent 1000 stretching cycles under 15% strain for the first four breaking and healing cycles. The fifth breaking cycle extended the number of cycles to 2500, during which the sensing performance remained stable. Moreover, the relative resistance changes of all specific sensing curves at the 1st stretch and release cycle before being broken, and right after conducting the breaking and healing process show similar trends (Fig. 4e). This behavior is indicative of good monotonicity, the ability to re-heal, and the efficiency of the re-healing process of the GO-AgNW/PVA-Ca<sup>2+</sup> strain sensor. To the best of the authors'

knowledge, this combination of sensitivity, stretchability, reliability, and effective healing ability, is the best reported for wearable strain sensors [7,16–18,62–67].

Following the studies, additional healing tests were conducted on the GO-AgNW/PVA-Ca<sup>2+</sup> strain sensor under cyclical strains of 3%, 10%, 30%, and 45%, as illustrated in Fig. 5. Following the breaking and subsequent healing process, it was confirmed that all devices with cyclical strain conditions spanning 3%–45% could be restored to their original state after being subjected to the water-initiated healing process. This further indicates the excellent healing capability of the GO-AgNW/PVA-Ca<sup>2+</sup> “brick-and-mortar” sensing materials.

For further validation of the healing efficacy of the GO-AgNW/PVA-Ca<sup>2+</sup> strain sensor, SEM images were taken during multiple steps of the testing process. Following the pre-conditioning step, microcracks and subsequent propagation can be observed throughout the nanocomposite film as a result of the brittle nature and layered architecture of the

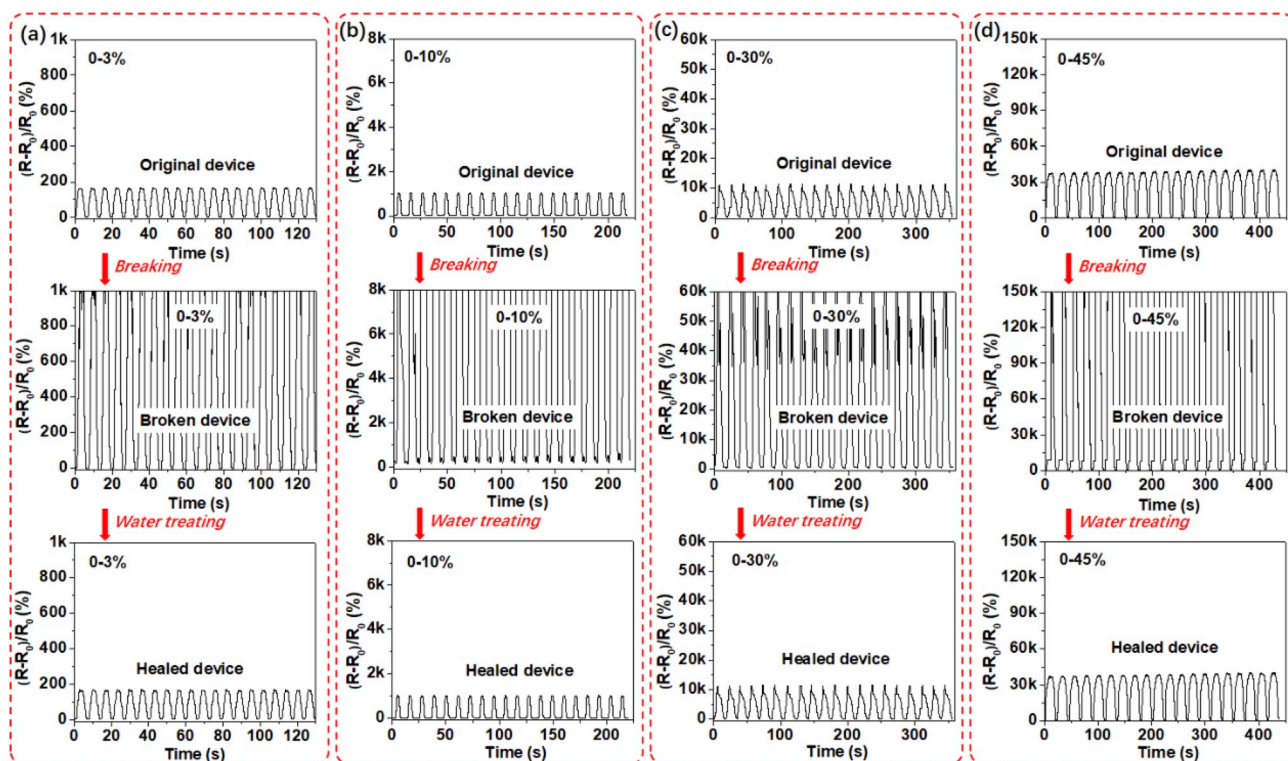


**Fig. 5.** Healing ability test for GO-AgNW/PVA-Ca<sup>2+</sup> strain sensor under various strains. Relative resistance variation under various cyclical maximum strains of (a) 3%, (b) 10%, (c) 30%, and (d) 45% for the GO-AgNW/PVA-Ca<sup>2+</sup> strain sensor before being broken, after being broken, and after being healed.

GO-AgNW “brick” material (Fig. 6a). These images are similar to those observed after 100 normal cycles of stretching and releasing under 15% strain (Fig. 6b), with uniformly distributed microcracks with slit edges in close contact with each other. The degree of cracking and propagation is limited due to interfacial hydrogen and coordination bonding, layer slippage, and molecular chain stretching of the “brick” and “mortar” materials, which toughen the sensor and enable the accommodation of higher applied strain [28,30,34–36,58–63]. After breaking the sensor, larger microcracks arise, manifesting in wider gaps and material detachment from the substrate (Fig. 6c), and ultimately resulting in device failure. Fig. 6d illustrates the broken sensing film after being treated with water and post-process annealed. The SEM image clearly depicts the reattachment of the separated slit edges, the disappearance of the gaps, and the reconnection of the AgNW network. The electrical manifestation of these physical observations results in complete restoration of the initial conductivity of GO-AgNW/PVA-Ca<sup>2+</sup> sensing film (Fig. S6).

Per the aforementioned discussion, the typical healing process is initiated when the following three conditions are met: 1) the fracture surfaces come closely in contact with each other; 2) the healable polymer chains migrate across the damaged interface; and 3) the dynamic interactions reconstruct at the damaged location [16,17,19,20,39,62]. Based on these criteria, a water-initiated healing mechanism for the GO-AgNW/PVA-Ca<sup>2+</sup> strain sensor is proposed and depicted in the schematic shown in Fig. 6e. When a droplet of water is initially applied onto the broken film, the hydrophilic nature of the sensing materials facilitates the wetting of the surface, leading to infiltration of water into the microcracks [37,41]. As such, water molecules are able to saturate the hydrogen bonds and solvate the Ca<sup>2+</sup> ions, decreasing the bonding constants of the hydrogen and coordination bonds and swelling the layered GO-PVA located at the crack edges [37]. This in turn leads to the generation of abundant free Ca<sup>2+</sup> ions and an increase in PVA chain mobility, enabling the interdiffusion of PVA

chains and Ca<sup>2+</sup> across the damaged interfaces [39,68]. The movement of the PVA chains is further accelerated by the heating process. In a separate process, the capillary force induced by water evaporation pushes the separated fracture surfaces closely together. Finally, after evaporation of the water, the interfused PVA chains bridge the damaged interface, allowing the dynamic hydrogen and coordination bonds to reform, leading to the restoration of sensing performance.

Based on the proposed healing mechanism, solvents with a low chemical affinity or solubility with PVA would not be able to trigger the healing process. To validate this hypothesis, various organic solvents including ethanol and acetone were used as healing agents to treat the broken GO-AgNW/PVA-Ca<sup>2+</sup> film. As a note, the solvents used had a similar viscosity to water, and were inert to PVA. As expected, no restoration of the sensing performance was observed (Fig. S7). To elucidate more details of the healing mechanism, 1 wt% aqueous solution of urea was also used in the healing test. Urea solution allows for the movement and interdiffusion of PVA chains and rebuilding of coordination bonds, but inhibits the restoration of hydrogen bonds. In the healing test, it was observed that the healing process prevailed for several breaking and healing cycles; however, the peak value in the relative resistance gradually increased with the number of cycles (Fig. S8). Lastly, the test was repeated with 1 wt% aqueous solution of Na<sub>2</sub>CO<sub>3</sub>, a solvent that inhibits both the rebuilding of hydrogen bonds and coordination bonds. The results of the healing test found that Na<sub>2</sub>CO<sub>3</sub> treated samples didn't exhibit any restoration in sensing performance (Fig. S9). The combined design of experiments indicates that the reformation of both hydrogen bonds and coordination bonds, and the chain movement of the PVA are responsible for the healing properties of the GO-AgNW/PVA-Ca<sup>2+</sup> sensing film.

To evaluate the healing performance of the healable, highly sensitive, and stretchable strain sensor under situations mimicking practical usage, the GO-AgNW/PVA-Ca<sup>2+</sup> strain sensor was adhered onto a human body to detect full-spectrum human motion. Two sensors were

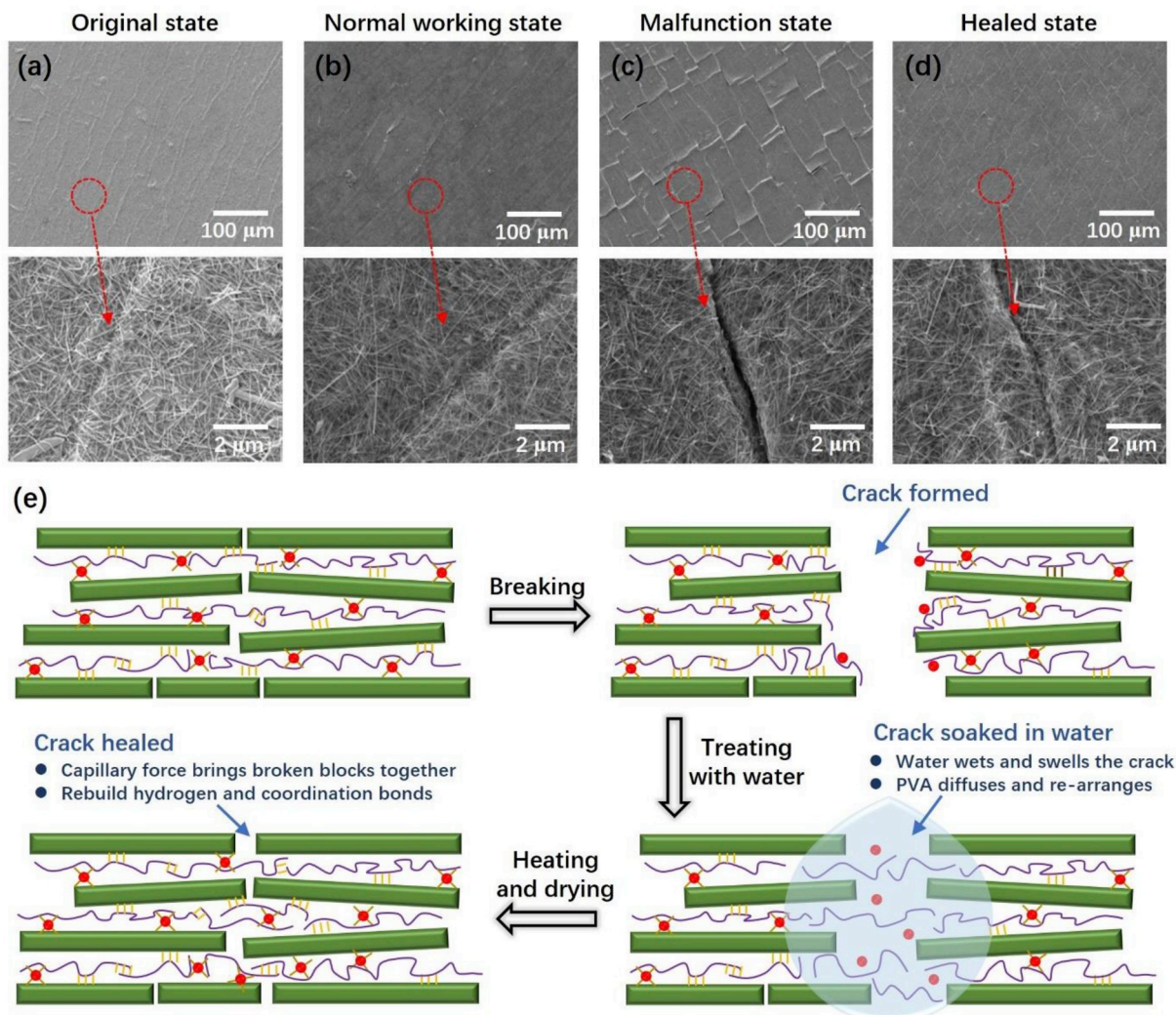


**Fig. 6.** Healing mechanism for the GO-AgNW/PVA-Ca<sup>2+</sup> strain sensor Typical and magnified surface SEM images for the GO-AgNW/PVA-Ca<sup>2+</sup> strain sensor (a) under its original state (right after pre-strain), (b) after normal operation of 100 stretching and releasing cycles between 0 and 15% strain, (c) under its broken state, and (d) under its healed state. (e) Schematic illustration of the water-initiated healing process of the GO-AgNW/PVA-Ca<sup>2+</sup> strain sensor.

attached onto the skin of a volunteer at the wrist and finger joint respectively, with the relative resistance change recorded to monitor the small strains from a wrist pulse, and large strains from a finger bending, as illustrated in Fig. 7. Before being broken, the high sensitivity afforded by the sensor enables precise detection of the pulse waveform clearly enough to resolve the electrical signals of the radial wave of a single heartbeat into the diastolic (D) wave, tidal (T) wave, and percussion (P) wave (Fig. 7a). In the separate demonstration, the large stretchability of the strain sensor allows the sensor to monitor the bending of the finger joint that requires repeatedly stretching to large strains (Fig. 7b). After intentionally breaking both sensors by overstretching, the variation in resistance becomes disordered and is no longer synchronized to the repeated motions of the wrist pulse and bending of the finger. However, once a droplet of water was applied onto the surface of the broken devices, followed by heating to initiate the healing process, the sensing ability was completely restored to both devices.

#### 4. Conclusions

A healable strain sensor was developed based on a microscale hierarchical architecture comprising PVA-Ca<sup>2+</sup> “mortar” material in

conjunction with GO-AgNW “brick” material. This healable strain sensor represents the first report of a device exhibiting the combined performance metrics obtained of high healing efficiency, remarkable re-healing capability, ultrahigh sensitivity, and large stretchability. The facile, water-initiated healing process opens up myriads of opportunities to enhance the durability and lifespan of wearable strain sensors. This unique and novel material design in conjunction with the cost-effective printing technology represents a concrete step forward towards its potential mass production and practical application in wearable electronics.

#### Progress and potential

The present work designs and constructs a skin-mountable and printable nanocomposite-based strain sensor with biomimetic hierarchical architecture, diffusible components, and abundant dynamic interactions which integrates the seemingly contradictory functionalities of effective healing capability (high healing efficiency over multiple breaking/healing cycles), large stretchability (working strain range > 50%), high sensitivity (gauge factor > 100 over the entire working strain range), and remarkable cycling durability. These performance metrics represent a solid step toward the practical application of

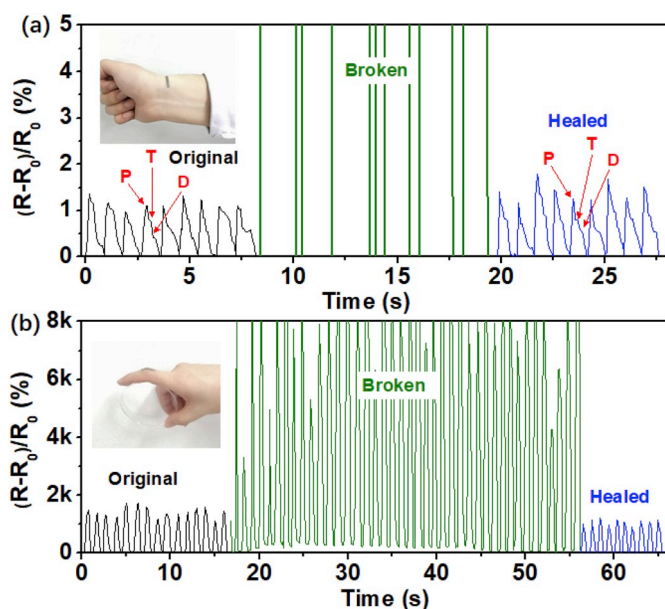


**Fig. 7.** Application for the healable GO-AgNW/PVA-Ca<sup>2+</sup> strain sensor. Demonstration of the healing process of the GO-AgNW/PVA-Ca<sup>2+</sup> strain sensor when used to monitor human motion, including (a) wrist pulse, and (b) finger bending.

wearable and durable strain sensors in full-range human-health diagnostics.

#### Acknowledgments

The work reported here was supported by NSFC (51872146, 51673099, 91633301, 21421001), Tianjin Municipal Science and Technology Commission (17JCZDJC30200) in China, and MOST (2016YFA0200200).

#### Appendix A. Supplementary data

Supplementary data to this article can be found online at <https://doi.org/10.1016/j.nanoen.2019.103898>.

#### References

- [1] W. Wu, H. Haick, *Adv. Mater.* 30 (2018) 1705024.
- [2] J. Kim, R. Kumar, A.J. Bandodkar, J. Wang, *Adv. Electron. Mater.* 3 (2017) 1600260.
- [3] G.-J.N. Wang, A. Gasperini, Z. Bao, *Adv. Electron. Mater.* 4 (2018) 1700429.
- [4] W. Liu, M.S. Song, B. Kong, Y. Cui, *Adv. Mater.* 29 (2017) 1603436.
- [5] X. Wang, Z. Liu, T. Zhang, *Small* 13 (2017) 1602790.
- [6] T.T. Tung, M.J. Nine, M. Krebsz, T. Pasinszki, C.J. Coghlan, D.N.H. Tran, D. Losic, *Adv. Funct. Mater.* 27 (2017) 1702891.
- [7] M. Amjadi, K.-U. Kyung, I. Park, M. Sitti, *Adv. Funct. Mater.* 26 (2016) 1678–1698.
- [8] Q. Liu, J. Chen, Y. Li, G. Shi, *ACS Nano* 10 (2016) 7901–7906.
- [9] L.-Q. Tao, K.-N. Zhang, H. Tian, Y. Liu, D.-Y. Wang, Y.-Q. Chen, Y. Yang, T.-L. Ren, *ACS Nano* 11 (2017) 8790–8795.
- [10] M. Amjadi, A. Pichitpajongkit, S. Lee, S. Ryu, I. Park, *ACS Nano* 8 (2014) 5154–5163.
- [11] D. Kang, P.V. Pikhitsa, Y.W. Choi, C. Lee, S.S. Shin, L. Piao, B. Park, K.-Y. Suh, T. Kim, M. Choi, *Nature* 516 (2014) 222.
- [12] Q. Zhang, S. Niu, L. Wang, J. Lopez, S. Chen, Y. Cai, R. Du, Y. Liu, J.-C. Lai, L. Liu, C.-H. Li, X. Yan, C. Liu, J.B.-H. Tok, X. Jia, Z. Bao, *Adv. Mater.* 30 (2018) 1801435.
- [13] R. Tamate, K. Hashimoto, T. Horii, M. Hirasawa, M. Shibayama, M. Watanabe, *Adv. Mater.* 30 (2018) 1802792.
- [14] J. Wu, L.-H. Cai, D.A. Weitz, *Adv. Mater.* 29 (2017) 1702616.
- [15] T. Wang, Y. Zhang, Q. Liu, W. Cheng, X. Wang, L. Pan, B. Xu, H. Xu, *Adv. Funct. Mater.* 28 (2018) 1705551.
- [16] G. Cai, J. Wang, K. Qian, J. Chen, S. Li, P.S. Lee, *Adv. Sci.* 4 (2017) 1600190.
- [17] S.J. Benight, C. Wang, J.B.H. Tok, Z. Bao, *Prog. Polym. Sci.* 38 (2013) 1961–1977.

- [18] Z. Lei, Q. Wang, S. Sun, W. Zhu, P. Wu, *Adv. Mater.* 29 (2017) 1700321.
- [19] Y.-J. Liu, W.-T. Cao, M.-G. Ma, P. Wan, *ACS Appl. Mater. Interfaces* 9 (2017) 25559–25570.
- [20] Y. Shi, M. Wang, C. Ma, Y. Wang, X. Li, G. Yu, *Nano Lett.* 15 (2015) 6276–6281.
- [21] J. Guo, X. Liu, N. Jiang, A.K. Yetisen, H. Yuk, C. Yang, A. Khademhosseini, X. Zhao, S.-H. Yun, *Adv. Mater.* 28 (2016) 10244–10249.
- [22] J.-C. Lai, J.-F. Mei, X.-Y. Jia, C.-H. Li, X.-Z. You, Z. Bao, *Adv. Mater.* 28 (2016) 8277–8282.
- [23] Z. Xiang, L. Zhang, Y. Li, T. Yuan, W. Zhang, J. Sun, *ACS Nano* 11 (2017) 7134–7141.
- [24] Y. Cao, H. Wu, S.I. Allec, B.M. Wong, D.-S. Nguyen, C.A. Wang, *Adv. Mater.* 30 (2018) 1804602.
- [25] Z. Liu, D. Qi, P. Guo, Y. Liu, B. Zhu, H. Yang, Y. Liu, B. Li, C. Zhang, J. Yu, B. Liedberg, X. Chen, *Adv. Mater.* 27 (2015) 6230–6237.
- [26] L. Li, H. Xiang, Y. Xiong, H. Zhao, Y. Bai, S. Wang, F. Sun, M. Hao, L. Liu, T. Li, Z. Peng, J. Xu, T. Zhang, *Adv. Sci.* 5 (2018) 1800558.
- [27] X. Shi, H. Wang, W. Yu, K. Wang, J. Wei, D. Wu, A. Cao, Z. Li, Y. Cheng, Q. Zheng, R.S. Ruoff, H. Zhu, *Sci. Rep.* 2 (2012) 870.
- [28] J. Peng, Q. Cheng, *Adv. Mater.* 29 (2017) 1702959.
- [29] Y. Zhang, J. Peng, M. Li, E. Saiz, S.E. Wolf, Q. Cheng, *ACS Nano* 12 (2018) 8901–8908.
- [30] W. Cui, M. Li, J. Liu, B. Wang, C. Zhang, L. Jiang, Q.A. Cheng, *ACS Nano* 8 (2014) 9511–9517.
- [31] Y. Wang, T. Li, P. Ma, S. Zhang, H. Zhang, M. Du, Y. Xie, M. Chen, W. Dong, W. Ming, *ACS Nano* 12 (2018) 6228–6235.
- [32] S. Wan, Q. Zhang, X. Zhou, D. Li, B. Ji, L. Jiang, Q. Cheng, *ACS Nano* 11 (2017) 7074–7083.
- [33] S. Park, K.-S. Lee, G. Bozoklu, W. Cai, S.T. Nguyen, R.S. Ruoff, *ACS Nano* 2 (2008) 572–578.
- [34] S. Wan, F. Xu, L. Jiang, Q. Cheng, *Adv. Funct. Mater.* 27 (2017) 1605636.
- [35] S. Wan, Y. Li, J. Peng, H. Hu, Q. Cheng, L. Jiang, *ACS Nano* 9 (2015) 708–714.
- [36] X. Shi, H. Wang, X. Xie, Q. Xue, J. Zhang, S. Kang, C. Wang, J. Liang, Y. Chen, *ACS Nano* 13 (2019) 649–659.
- [37] H. Cheng, Y. Huang, Q. Cheng, G. Shi, L. Jiang, L. Qu, *Adv. Funct. Mater.* 27 (2017) 1703096.
- [38] H. Zhang, H. Xia, Y. Zhao, *ACS Macro Lett.* 1 (2012) 1233–1236.
- [39] D.L. Taylor, M. in het Panhuis, *Adv. Mater.* 28 (2016) 9060–9093.
- [40] S. Liu, J. Li, X. Shi, E. Gao, Z. Xu, H. Tang, K. Tong, Q. Pei, J. Liang, Y. Chen, *Adv. Electron. Mater.* 3 (2017) 1700098.
- [41] X. Shi, S. Liu, Y. Sun, J. Liang, Y. Chen, *Adv. Funct. Mater.* 28 (2018) 1800850.
- [42] C. Wang, X. Li, E. Gao, M. Jian, K. Xia, Q. Wang, Z. Xu, T. Ren, Y. Zhang, *Adv. Mater.* 28 (2016) 6640–6648.
- [43] J. Liang, Y. Huang, L. Zhang, Y. Wang, Y. Ma, T. Guo, Y. Chen, *Adv. Funct. Mater.* 19 (2009) 2297–2302.
- [44] O.C. Compton, S.W. Cranford, K.W. Putz, Z. An, L.C. Brinson, M.J. Buehler, S.T. Nguyen, *ACS Nano* 6 (2012) 2008–2019.
- [45] H. Bai, C. Li, X. Wang, G. Shi, *Chem. Commun.* 46 (2010) 2376–2378.
- [46] J.B. Lambert, H.F. Shurvell, D.A. Lightner, R.G. Cooks, *Organic Structural Spectroscopy*, second ed., Prentice Hall, New York, 2001, pp. 189–196.
- [47] M. Acik, G. Lee, C. Mattevi, M. Chhowalla, K. Cho, Y. Chabal, *J. Nat. Mater.* 9 (2010) 840.
- [48] K. Nakamoto, *Infrared and Raman Spectra of Inorganic and Coordination Compounds*, fourth ed., John Wiley & Son, New York, 1986, pp. 231–233.
- [49] R.E. Parker, N.S. Isaacs, *Chem. Rev.* 59 (1959) 737–799.
- [50] S.-H.J. Rhee, *Biomater. Sci. Polymer Edn.* 21 (2010) 1127–1141.
- [51] X. Jiang, T. Jiang, L. Gan, X. Zhang, H. Dai, X. Zhang, *Carbohydr. Polym.* 90 (2012) 1677–1684.
- [52] A.A. Bonapasta, F. Buda, P. Colombet, G. Guerrini, *Chem. Mater.* 14 (2002) 1016–1022.
- [53] S. Zhang, Z. Lin, G. Jiang, J. Wang, D.-Y. Wang, *Compos. Sci. Technol.* 159 (2018) 59–69.
- [54] C.S. Boland, U. Khan, G. Ryan, S. Barwich, R. Charifou, A. Harvey, C. Backes, Z. Li, M.S. Ferreira, M.E. Möbius, R.J. Young, J.N. Coleman, *Science* 354 (2016) 1257.
- [55] C.S. Boland, U. Khan, C. Backes, A. O'Neill, J. McCauley, S. Duane, R. Shanker, Y. Liu, I. Jurewicz, A.B. Dalton, J.N. Coleman, *ACS Nano* 8 (2014) 8819–8830.
- [56] C. Yan, J. Wang, W. Kang, M. Cui, X. Wang, C.Y. Foo, K.J. Chee, P.S. Lee, *Adv. Mater.* 26 (2014) 2022–2027.
- [57] J. Zhou, X. Xu, Y. Xin, G. Lubineau, *Adv. Funct. Mater.* 28 (2018) 1705591.
- [58] J. Wang, Q. Cheng, L. Lin, L. Jiang, *ACS Nano* 8 (2014) 2739–2745.
- [59] Q. Cheng, L. Jiang, Z. Tang, *Acc. Chem. Res.* 47 (2014) 1256–1266.
- [60] Y. Cheng, J. Peng, H. Xu, Q. Cheng, *Adv. Funct. Mater.* 28 (2018) 1800924.
- [61] S. Gong, Q. Cheng, *Compos. Commun.* 7 (2018) 16–22.
- [62] X. Liu, C. Lu, X. Wu, X. Zhang, *J. Mater. Chem.* 5 (2017) 9824–9832.
- [63] Y. Han, X. Wu, X. Zhang, C. Lu, *ACS Appl. Mater. Interfaces* 9 (2017) 20106–20114.
- [64] M. Liao, P. Wan, J. Wen, M. Gong, X. Wu, Y. Wang, R. Shi, L. Zhang, *Adv. Funct. Mater.* 27 (2017) 1703852.
- [65] M.A. Darabi, A. Khosrozadeh, R. Mbeleck, Y. Liu, Q. Chang, J. Jiang, J. Cai, Q. Wang, G. Luo, M. Xing, *Adv. Mater.* 29 (2017) 1700533.
- [66] X. Liao, Q. Liao, X. Yan, Q. Liang, H. Si, M. Li, H. Wu, S. Cao, Y. Zhang, *Adv. Funct. Mater.* 25 (2015) 2395–2401.
- [67] M. Zhang, C. Wang, H. Wang, M. Jian, X. Hao, Y. Zhang, *Adv. Funct. Mater.* 27 (2017) 1604795.
- [68] N.N. Xia, X.M. Xiong, J. Wang, M.Z. Rong, M.Q. Zhang, *Chem. Sci.* 7 (2016) 2736–2742.



**Yang Liu** is currently a Ph.D. candidate in School of Material Science and Engineering under the supervision of Prof. Jiajie Liang at Nankai University. He received his B.S. degree from Shandong Agriculture University in 2014 and M.S. degree from Nankai University in 2017. His current research interests focus on wearable and stretchable devices.



**Huailong Zhang** received his B.S. degree in Materials Physics and Chemistry from Nankai University. His research interests focus on strain sensors.



**Xinlei Shi** received his B.S. degree in physics from Shandong University of Science and Technology in 2016. He is pursuing his Ph.D. degree under the direction of Prof. Jiajie Liang at Nankai University. His current research interests include flexible and highly sensitive strain sensors.



**Conghui Wang** received her B.S. degree in Chemical Engineering and Technology from Xinjiang University. She is pursuing M.S. degree under the supervision of Prof. Jiajie Liang at Nankai University.



**Shuiren Liu** received his M.S. degree in chemistry from Beijing University of Chemical Technology. He obtained Ph.D. degree in Materials Physics and Chemistry from Nankai University under the supervision of Prof. Jiajie Liang. His current research interests focus on conductive ink and foldable, stretchable electronics.



**Prof. Jiajie Liang** received his B.S. degree in chemistry from Nankai University in 2006. He obtained his Ph.D. degree in polymer chemistry and physics from Nankai University in 2011 under the supervision of Prof. Yongsheng Chen. He worked as a postdoctoral researcher in Prof. Qibing Pei's group at the University of California, Los Angeles, from 2011 to 2016. Thereafter, he joined Nankai University as a full professor and started to build the Lab for Printed and Wearable Electronics at the School of Materials Science & Engineering.



**Hongpeng Li** is currently a Ph.D. candidate in School of Material Science and Engineering at Nankai University under the direction of Prof. Jiajie Liang. He received his B.S. degree in Department of Applied Chemistry from Jilin Institute of Chemical Technology in 2013 and M.S. degree in Chemical Engineering and Technology from Harbin Engineering University in 2016. His current research interests focus on the design and fabrication of high-performance energy storage devices.



**Prof. Yongsheng Chen** graduated from University of Victoria with Ph.D. in chemistry in 1997 with Prof. Reg Mitchell and joined Prof. Robert Haddon/Peter Eklund and Prof. Fred Wudl groups for postdoctoral study from 1997-1999. His current research interests focus on multi-functional materials based on carbon nanotubes and graphene, organic and polymeric functional materials, and green energy devices.